Fine-Scale Turbulence Noise from Dual-Stream Jets

Christopher K. W. Tam* and Nikolai N. Pastouchenko†

Florida State University, Tallahassee, Florida 32306-4510

Nowadays, commercial aircrafts, invariably, use high-bypass-ratio dual-stream jets for propulsion. As yet, there is still an urgent need for an accurate physics-based noise prediction theory for jets of this configuration. Thus, an investigation is made to determine whether the Tam and Auriault theory (Tam, C. K. W., and Auriault, L., "Jet Mixing Noise from Fine Scale Turbulence," *AIAA Journal*, Vol. 37, No. 2, 1999, pp. 145–153), originally developed for predicting the fine-scale turbulence noise of single-stream jets, is capable of predicting accurately the fine-scale turbulence noise of dual-stream jets from separate flow nozzles operating at various bypass ratios. The configuration of a separate flow nozzle is fairly complex. Hence, the jet flow and turbulence in the nozzle region and in the region immediately downstream are also fairly complex. However, these are also the most important noise source regions of the jet. To enable an accurate computation of the mean flow and turbulence level in these regions, a computational aeroacoustics marching algorithm for calculating the parabolized Reynolds averaged Navier–Stokes equations supplemented by the k–ε turbulence model is provided. It is shown that the computed mean flow profiles are in good agreement with experiment. Extensive comparisons between computed noise spectra and measurements are reported. They include dual-stream jets from separate flow nozzles with and without an external plug. Jets operating at different combinations of primary and secondary jet Mach number and temperature ratio are considered. The bypass ratios range from 1.5 to 8.0. Effects of forward flight are also included in the comparisons. Good agreements are found not only in spectral levels but also in spectrum shapes and directivities over many sets of data.

I. Introduction

PRESENT day commercial jet engines, invariably, use dual-stream nozzles. The nozzle configuration can be fairly complex. In most cases, the secondary nozzle is recessed back relative to the primary nozzle. A popular design often includes an external plug for the primary nozzle. The nozzle geometry of a dual-stream jet has an important influence on the mixing and spatial evolution of the jet flow. In turn, they exert a significant impact on the intensity and spectral distribution of the noise radiated by the jet.

It is now established that there are large turbulence structures[1,2] and fine-scale turbulence in a jet flow. The noise generated by the large turbulence structures and that by the fine-scale turbulence are different in directivity and spectral content.[3−6] The purpose of this investigation is to establish a theoretical/computational framework by which the fine-scale turbulence noise of jets from dual-stream nozzles can be calculated.

Panda and Seasholtz[7] and Panda et al.,[8] in a recent series of experiments, appear to have provided the most direct evidence that there are two sources of jet noise. One source of noise is the large-scale turbulence in the jet flow. The principal direction of radiation is in the downstream direction. The other source is the fine-scale turbulence. This is the dominant noise component for radiation to the sideline and upstream directions. Panda and Seasholtz[7] and Panda et al.[8] used a technique based on Rayleigh scattering to measure the turbulent velocity and density fluctuations in a very localized volume (almost point-like measurement) inside a jet. They correlated this signal with the acoustic pressure measured by a far-field microphone to determine the source of noise. They found significant normalized correlations for pointlike measurements at the end of the potential core of the jet and far-field microphone at 30 deg (exhaust angle). The normalized correlations for jets at Mach numbers 1.8, 1.4, and 0.95 were 22, 19, and 7%, respectively. The correlations maintained at about the same level when the measurement point inside the jet was moved radially over the half-width of the jet and axially over a distance of a few jet diameters. On the other hand, when the far-field microphone was at 90 deg, the correlation dropped to a very low level (little correlation). Note that a far-field microphone receives noise from all sources in a jet. If the sources are small and localized, the correlation of far-field pressure with turbulence fluctuations of a small blob of turbulence would be statistically insignificant. This is the case of noise radiated by the fine-scale turbulence to the microphone at 90 deg. However, the strong correlation measured at 30 deg requires that the noise source be coherent over a sizable volume. In this case, a good fraction of the noise receives by the far microphone comes from the large coherent source. The experimental results of Panda et al.[8] are consistent with the earlier observations of Hurdle et al.[9] (Mach 0.99 and 0.85 jets) and Schaffar[10] (Mach 0.98 jet). In addition, the more recent correlation measurements by Bogey and Bailly[11] using numerical simulation data computed by large-eddy simulation methodology also yielded very similar conclusions. Evidently, all of these results are in support of the suggestion[3−6] that there are two noise sources in a high-speed jet. The dominant source that is responsible for radiation in the downstream directions is the large-scale turbulence, whereas that in the sideline direction is the fine-scale turbulence.

In a recent work, Tam and Auriault[12] developed a fine-scale turbulence noise prediction theory for single-stream jets. The noise source of the theory is the time fluctuation of the fine-scale turbulence intensity. The theory also accounts for the source convection effect, as well as the mean flow refraction effect. The turbulence information required by the theory, including turbulence intensity, timescale and spatial scale of fine-scale turbulence, are provided by the k–ε turbulence model. Extensive comparisons between computed noise spectra by the theory and experimental measurements have been carried out over a large range of jet Mach numbers and jet temperature ratios. Jets from nonaxisymmetric nozzles[13] as well as jets in simulated forward flight[14] were also considered. Favorable agreements were found for cold to moderate temperature jets.

It is known that because of the existence of a large density gradient in hot jets, the standard k–ε turbulence model is inadequate for

*Robert O. Lawton Distinguished Professor, Department of Mathematics. Fellow AIAA.

†Postdoctoral Research Associate, Department of Mathematics.

predicting the evolution of the mean flow. The reasons for the inadequacy were recently investigated by Tam and Ganesan.[15] Based on their findings, they proposed a modification to the k–ε turbulence model to remedy the shortcomings of the original model. Hot jet mean flows calculated by the modified k–ε model were found to agree well with experiments. The existence of a large density gradient in hot jets also affects the noise source strength and characteristics. Doty and McLaughlin[16] have measured two-point space–time density gradient fluctuation correlation functions showing that the noise source function for hot jets is qualitatively different from that for cold jets. On taking into consideration the needed changes in the k–ε turbulence model for the mean flow and turbulence calculation and by adopting a more general noise source function for hot jets, Tam et al.[17] recently extended the Tam and Auriault jet noise theory to hot jets. They showed that their extended jet noise theory was capable of predicting the noise spectra of hot single jets accurately over a wide range of Mach numbers and temperature ratios.

In this work, the extended fine-scale turbulence noise theory of Tam et al.[17] is applied, without any modification, to jets from dual-stream nozzles. For jet flow calculations, the same modified k–ε turbulence model used by Tam and Ganesan[15] for their single-stream hot jet computations is employed here without change. A set of parabolized Reynolds averaged Navier–Stokes (RANS) equations and a computer code using the modified k–ε turbulence model are developed for calculating the jet mean flow and turbulence scales and levels of dual-stream jets. The computation scheme uses a body-fitted oblique Cartesian mesh. The computation starts at the exit of the secondary (fan) nozzle and marches downstream. The code has been found to be very efficient. Here details of the parabolized equations, the computation mesh, and marching algorithm will be reported. The computed mean flow profiles are compared with experimental measurements. Good agreements are found. The computed mean flow and k–ε turbulence information are then used as input for jet noise prediction through the extended jet noise theory. Extensive comparisons between the calculated noise spectra at inlet angles from 50 to 110 deg and measured data from the NASA Langley Research Center and The Boeing Company are presented in this paper. Jets issuing from nozzles with and without an external plug are included in the study. Measured data with simulated forward flight in an open wind tunnel are also used for comparisons. Good agreements between the computed noise spectra and experimental measurements are found in all cases.

II. Computation of Nozzle Flow

The first step in computing the fine-scale turbulence noise of a dual-stream jet by the Tam and Auriault theory[12] is to calculate the jet mean flow and relevant turbulence information. Given that the nozzle geometry of these jets is fairly complex, such a computation is not straightforward but is a rather demanding task. Figures 1a and 1b are schematic diagrams of typical separate flow nozzles of dual-stream jets with and without an external plug used in commer-
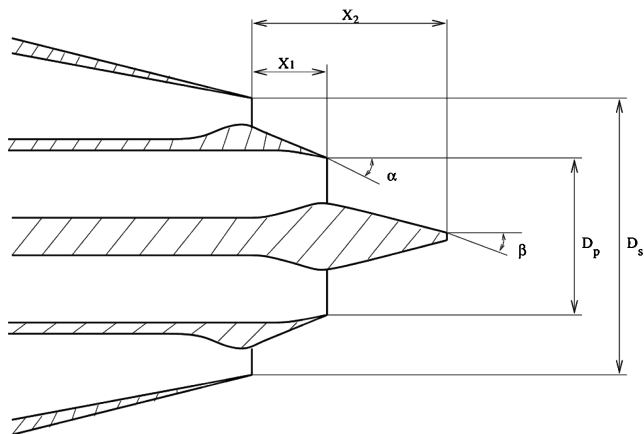

Fig. 1a   Schematic of an axisymmetric dual-stream nozzle with external plug.
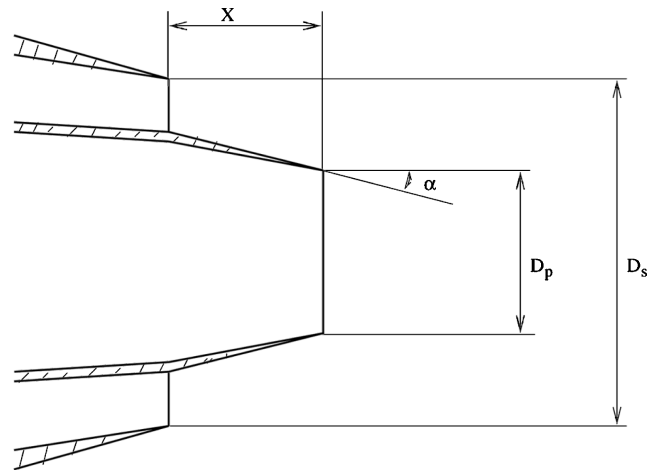

Fig. 1b   Schematic of an axisymmetric dual-stream nozzle with no external plug.

cial aircraft engines. Most dual-stream nozzles are designed so that the flow is unimpeded in the downstream direction. This suggests that the nozzle geometrical parameters are chosen such that the jet flow exerts its influence primarily in the downstream direction. In other words, there is very little upstream influence. Under this circumstance, a parabolized marching computation of the mean flow profile is permissible.

Computations of the mean flows of dual-stream jets were carried out recently by Georgiadis and Papamouschou,[18] Birch et al.,[19] and others. Georgiadis and Papamouschou confined their calculations to nozzles without a center plug. Birch et al. found difficulties in selecting turbulence models that would give accurate predictions for the flow of even a simple axisymmetric jets. They introduced a new zonal model for their jet flow calculations. However, they recognized that their turbulence model might have only a limited range of applicability. Note that the flows of dual-stream jets in commercial aircraft engines are, invariably, modified by the presence of a bifurcation and noise suppression devices; for example, see Bhat,[20] Nesbitt et al.,[21] Mead and Strange,[22] and Blackner and Bhat.[23] In this work, only axisymmetric nozzles are considered.

For separate flow nozzles, the jet flow is essentially parallel to the nozzle wall. This fact will be taken advantage of in deriving the governing parabolized mean flow equations. Adjacent to the nozzle wall is a turbulent boundary layer. A complete resolution of the turbulent boundary-layer profile all of the way to the wall would require an exceedingly large number of mesh points. This is not feasible for a practical jet noise computation. Fortunately, for noise prediction purposes, the details of the turbulent boundary layer are not important. This is because most of the noise is generated by the turbulence in the free mixing layer between the secondary jet and the ambient gas and the mixing layer in between the primary and the secondary jet. Wall bounded turbulence is not an important source of jet noise. In this work, as an approximation, a slip boundary condition will be used at the nozzle walls in lieu of a turbulent boundary layer. This is a reasonable approximation because the length of the nozzle wall is short so that the boundary-layer thickness remains very thin to the end of the wall.

In practice, the walls of separate flow nozzles, over which the secondary and the primary jet fluids flow, are straight. This will be assumed to be the case. If this is not true, an extra mapping may be performed to transform the curved wall to a straight wall for computational purposes. For axisymmetric separate flow nozzles as shown in Fig. 1, we propose to divide the computation domain into three regions as indicated in Fig. 2. Region 3, which is downstream of the nozzle, has no solid boundaries. The computation may be carried out with existing parabolized mean flow algorithms.[15,24] Here we will consider only the development of a marching algorithm for mean flow computation in regions 1 and 2. The parabolized computation will start at the exit of the secondary jet. That is, at the upstream end
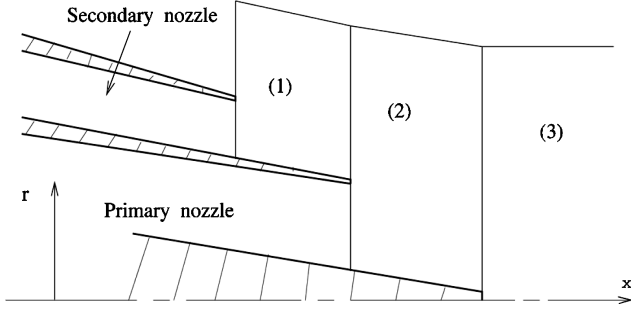
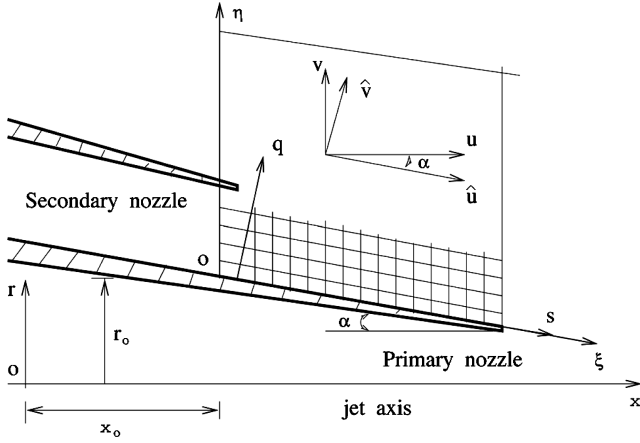**Fig. 2   Computational domains for calculating mean flow of a separate flow nozzle using a marching algorithm.**

Fig. 3   Oblique Cartesian coordinates and local velocity component $(\hat{u}, \hat{v})$.

of region 1. At this location, the mean flow conditions are given by the exit parameters of the secondary jet. The marching algorithm will use them as the starting conditions and compute the solution in the downstream direction until the end of region 1 is reached. At the upstream end of region 2, the exit conditions of the primary jet are taken to be given by the design values. With this input and the solution in region 1, the starting conditions for region 2 are now complete. The mean flow computation may proceed downstream through region 2 until region 3 is reached. For many nozzle designs, the tip of the external plug is not pointed. A special treatment of the flow just downstream of a blunt tip is required in computing the mean flow in region 3. This will be discussed later.

A.   Oblique Cartesian Coordinates

For the convenience of enforcing the no-flow penetration boundary condition at the nozzle wall and the imposition of boundary-layer-type approximation to the governing equations, the local velocity component $(\hat{u}, \hat{v})$ in directions s and q will be used instead of the regular velocity component (u, v) in cylindrical coordinates (r, ϕ, x) as shown in Fig. 3. The s axis coincides with the nozzle wall on the plane $\phi = $ constant. The q axis is normal to the nozzle wall. The relationships between (u, v) and $(\hat{u}, \hat{v})$ are

$$u = \hat{u}\cos\alpha + \hat{v}\sin\alpha, \qquad v = -\hat{u}\sin\alpha + \hat{v}\cos\alpha \qquad (1)$$

where α is the angle of inclination of the nozzle wall with respect to the x axis. The corresponding relationships between turbulent stress components are

$$\tau_{rr} = \tau_{ss}\sin^2\alpha - \tau_{sq}\sin(2\alpha) + \tau_{qq}\cos^2\alpha$$

$$\tau_{xx} = \tau_{ss}\cos^2\alpha + \tau_{sq}\sin(2\alpha) + \tau_{qq}\sin^2\alpha$$

$$\tau_{rx} = \tau_{xr} = -\tau_{ss}\sin\alpha\cos\alpha + \tau_{sq}\cos(2\alpha) + \tau_{qq}\sin\alpha\cos\alpha \quad (2)$$

A natural set of local coordinates useful for computing the jet mean flow in region 1 is the oblique Cartesian coordinates (ξ, η) as shown in Fig. 3. The origin of this coordinate system is at O where the cylindrical coordinates are (r_0, x_0). The oblique Cartesian coordinates (ξ, η) are related to the cylindrical coordinates by

$$\eta = (r - r_0) + (x - x_0)\tan\alpha, \qquad \xi = (x - x_0)/\cos\alpha \quad (3)$$

The inverse is

$$x = \xi\cos\alpha + x_0, \qquad r = \eta - \xi\sin\alpha + r_0 \qquad (4)$$

B.   Parabolized RANS Equations in Oblique Cartesian Coordinates

We consider the RANS equations with the k–ε turbulence model as the governing equations of the mean flow of the jet. To cast these equations into a parabolized form, the first step is to write out the full set of equations in cylindrical coordinates. The second step is to perform a change of variables from (u, v) to $(\hat{u}, \hat{v})$ by means of Eq. (1). Similarly the stress components are replaced by the stress components in the local coordinates by Eq. (2). The next step is to transform the partial derivative from (r, x) to (ξ, η) as follows:

$$\frac{\partial}{\partial r} = \frac{\partial}{\partial \eta}, \qquad \frac{\partial}{\partial x} = \frac{1}{\cos\alpha}\frac{\partial}{\partial \xi} + \tan\alpha\frac{\partial}{\partial \eta} \qquad (5)$$

Now it will be assumed that the jet flow is locally quasi parallel so that $\partial/\partial\xi$ is small. This allows us to retain only the first derivative terms in ξ and to drop all terms with higher ξ derivatives. To reduce the number of equations in the system, the equation of state is used to eliminate density ρ in favor of pressure p and temperature T. When nondimensional variables are used with L_{ref} as the length scale, u_{ref} as the velocity scale, $L_{\text{ref}}/u_{\text{ref}}$ as the timescale, ρ_{ref} as the density scale, $\rho_{\text{ref}}u_{\text{ref}}^2$ as the pressure scale, T_{ref} as the temperature scale, u_{ref}^2 as the scale for k and τ_{ij} (although the actual turbulence stresses are $\rho\tau_{ij}$), $u_{\text{ref}}^3/L_{\text{ref}}$ as scale for ε, and $L_{\text{ref}}u_{\text{ref}}$ as scale for ν_t (the turbulent eddy viscosity), the parabolized dimensionless RANS equations in oblique Cartesian coordinates may be written out in full as

$$\frac{\partial \hat{u}}{\partial \xi} = \frac{1}{\hat{u} + \hat{v}\tan\alpha}\left[-\frac{\hat{v}}{\cos\alpha}\frac{\partial \hat{u}}{\partial \eta} - \frac{1}{\rho\cos\alpha}\frac{\partial}{\partial \eta}(\rho\tau_{sq}) \right.$$

$$\left. + \frac{1}{r}(\tau_{ss}\sin\alpha - \tau_{sq}\cos\alpha - \tau_{\phi\phi}\sin\alpha) \right] \qquad (6)$$

$$\frac{\partial \hat{v}}{\partial \xi} = \frac{1}{\hat{u} + \hat{v}\tan\alpha}\left[-\frac{1}{\rho\cos\alpha}\frac{\partial p}{\partial \eta} - \frac{\hat{v}}{\cos\alpha}\frac{\partial \hat{v}}{\partial \eta} - \frac{1}{\rho\cos\alpha}\frac{\partial}{\partial \eta}(\rho\tau_{qq}) \right.$$

$$\left. + \frac{1}{r}(\tau_{sq}\sin\alpha - \tau_{qq}\cos\alpha + \tau_{\phi\phi}\cos\alpha) \right] \qquad (7)$$

$$\frac{\partial T}{\partial \xi} = \frac{1}{\hat{u} + \hat{v}\tan\alpha}\left(-\frac{\hat{v}}{\cos\alpha}\frac{\partial T}{\partial \eta} - \gamma(\gamma - 1)M_{\text{ref}}^2\frac{p}{\rho}\left[\frac{\partial \hat{u}}{\partial \xi} + \frac{1}{\cos\alpha}\frac{\partial \hat{v}}{\partial \eta} \right] \right.$$

$$+ \frac{1}{r}(-\hat{u}\sin\alpha + \hat{v}\cos\alpha) \right] + \gamma(\gamma - 1)M_{\text{ref}}^2\varepsilon + \frac{\gamma}{Pr}$$

$$\times \left\{ \tan^2\alpha\frac{\partial}{\partial \eta}\left(\nu_t\frac{\partial T}{\partial \eta} \right) + \frac{1}{r}\frac{\partial}{\partial \eta}\left[(\eta - \xi\sin\alpha + r_0)\nu_t\frac{\partial T}{\partial \eta} \right] \right\} \right)$$

$$(8)$$

$$\frac{\partial p}{\partial \xi} = \frac{1}{\hat{u} + \hat{v}\tan\alpha}\left[(\hat{u} + \hat{v}\tan\alpha)\frac{p}{T}\frac{\partial T}{\partial \xi} - p\left(\frac{\partial \hat{u}}{\partial \xi} + \frac{1}{\cos\alpha}\frac{\partial \hat{v}}{\partial \eta} \right) \right.$$

$$\left. - \frac{\hat{v}}{\cos\alpha}\frac{\partial p}{\partial \eta} + \frac{p\hat{v}}{\cos\alpha T}\frac{\partial T}{\partial \eta} + \frac{p}{r}(\hat{u}\sin\alpha - \hat{v}\cos\alpha) \right] \qquad (9)$$

$$\frac{\partial k}{\partial \xi} = \frac{1}{\hat{u} + \hat{v}\tan\alpha}\left(-\frac{\hat{v}}{\cos\alpha}\frac{\partial k}{\partial \eta} - \frac{\tau_{sq}}{\cos\alpha}\frac{\partial \hat{u}}{\partial \eta} - \frac{\tau_{qq}}{\cos\alpha}\frac{\partial \hat{v}}{\partial \eta}\right.$$

$$-\frac{\tau_{\phi\phi}}{r}(-\hat{u}\sin\alpha + \hat{v}\cos\alpha) - \varepsilon + \frac{1}{\rho\sigma_k}$$

$$\left.\times\left\{\frac{1}{r}\frac{\partial}{\partial \eta}\left[(\eta - \xi\sin\alpha + r_0)\rho\nu_t\frac{\partial k}{\partial \eta}\right] + \tan^2\alpha\frac{\partial}{\partial \eta}\left(\rho\nu_t\frac{\partial k}{\partial \eta}\right)\right\}\right)$$

$$(10)$$

$$\frac{\partial \varepsilon_s}{\partial \xi} = \frac{1}{\hat{u} + \hat{v}\tan\alpha}\left(-\frac{\hat{v}}{\cos\alpha}\frac{\partial \varepsilon_s}{\partial \eta} - C_{\varepsilon 1}\frac{\varepsilon_s}{k}\left[\frac{\tau_{sq}^{(s)}}{\cos\alpha}\frac{\partial \hat{u}}{\partial \eta} + \frac{\tau_{qq}^{(s)}}{\cos\alpha}\frac{\partial \hat{v}}{\partial \eta}\right.\right.$$

$$\left.+ \frac{\tau_{\phi\phi}^{(s)}}{r}(-\hat{u}\sin\alpha + \hat{v}\cos\alpha)\right] - (C_{\varepsilon 2} - \chi C_{\varepsilon 3})\frac{\varepsilon_s^2}{k}$$

$$+ \frac{1}{\rho\sigma_\varepsilon}\left\{\frac{1}{r}\frac{\partial}{\partial \eta}\left[(\eta - \xi\sin\alpha + r_0)\rho\nu_t^{(s)}\frac{\partial \varepsilon_s}{\partial \eta}\right]\right.$$

$$\left.\left.+ \tan^2\alpha\frac{\partial}{\partial \eta}\left(\rho\nu_t^{(s)}\frac{\partial \varepsilon_s}{\partial \eta}\right)\right\}\right)$$

$$(11)$$

$$\chi = -\frac{k^3}{4\varepsilon_s^3}\left[-\tan\alpha\frac{\partial \hat{u}}{\partial \xi} + \frac{\partial \hat{v}}{\partial \xi} - \frac{1}{\cos\alpha}\frac{\partial \hat{u}}{\partial \eta}\right]^2$$

$$\times\left[-\sin\alpha\frac{\partial \hat{u}}{\partial \eta} + \cos\alpha\frac{\partial \hat{v}}{\partial \eta} + \frac{1}{r}(-\hat{u}\sin\alpha + \hat{v}\cos\alpha)\right] \quad (12)$$

$$\varepsilon = \varepsilon_s\left(1 + \alpha_1 M_t^2\right), \qquad M_t^2 = \frac{2k}{T}M_{\text{ref}}^2, \qquad \rho = \frac{p}{T}\gamma M_{\text{ref}}^2 \quad (13)$$

$$\text{tr} = \frac{1}{\cos\alpha}\frac{\partial \hat{v}}{\partial \eta} - \frac{1}{r}\hat{u}\sin\alpha + \frac{1}{r}\hat{v}\cos\alpha$$

$$\tau_{ss} = \frac{2}{3}k + \frac{2}{3}\nu_t(\text{tr}), \qquad \tau_{qq} = \frac{2}{3}k - 2\nu_t\left(\frac{1}{\cos\alpha}\frac{\partial \hat{v}}{\partial \eta} - \frac{1}{3}\text{tr}\right)$$

$$\tau_{sq} = -\frac{\nu_t}{\cos\alpha}\frac{\partial \hat{u}}{\partial \eta} \quad (14)$$

$$\tau_{\phi\phi} = \frac{2}{3}k - 2\nu_t\left[\frac{1}{r}(-\hat{u}\sin\alpha + \hat{v}\cos\alpha) - \frac{1}{3}\text{tr}\right]$$

$$\nu_t = C_\mu\frac{k^2}{\varepsilon} + \nu_\rho$$

$$\nu_\rho = \begin{cases} C_\rho\frac{k^{\frac{7}{2}}}{\varepsilon^2}\frac{1}{\rho}\frac{\partial \rho}{\partial \eta}, & \text{if} \quad \frac{\partial \rho}{\partial \eta} \text{ and } \frac{\partial \hat{u}}{\partial \eta} \text{ have opposite signs} \\ 0, & \text{otherwise} \end{cases} \quad (15)$$

where $\tau_{ij}^{(s)}$ and $\nu_t^{(s)}$ are the same as τ_{ij} and ν_t with ε_s replacing ε. There are nine empirical constants. Here the values recommended by Thies and Tam[24] and Tam and Ganesan[15] are adopted:

$$C_\mu = 0.0874, \qquad C_{\varepsilon 1} = 1.40, \qquad C_{\varepsilon 2} = 2.02, \qquad C_{\varepsilon 3} = 0.822$$

$$\gamma\sigma_T = Pr = 0.422, \qquad \sigma_k = 0.324, \qquad \sigma_\varepsilon = 0.377$$

$$\alpha_1 = 0.518, \qquad C_\rho = 0.035$$

where $M_{\text{ref}} = u_{\text{ref}}/(\gamma R T_{\text{ref}})^{1/2}$ and γ is the ratio of specific heats. In the derivation of Eq. (6), a $\partial p/\partial \xi$ term on the right-hand side is omitted. This is necessary to eliminate upstream influence due to the compressibility effect so that the system of equations is parabolic. In the derivation of Eqs. (8) and (9), a boundary-layer-type approximation has been invoked. Instead of the term $(1/\cos\alpha)(\partial\hat{v}/\partial\eta)$

on the right-hand side of the equations, there are two terms, that is, $[(1/\cos\alpha)(\partial\hat{v}/\partial\eta) + \tan\alpha(\partial\hat{v}/\partial\xi)]$ originally. However, boundary-layer argument suggests that $(\partial\hat{v}/\partial\eta) \gg (\partial\hat{v}/\partial\xi)$. For this reason, the $\tan\alpha(\partial\hat{v}/\partial\xi)$ term is dropped in both equations. It turns out by neglecting this term there is an improvement on the numerical stability of the system of equations. This allows the use of a larger marching step in the ξ direction.

When the preceding system of equations is computed as a set of parabolized equations in ξ, it is assumed that there is an outside flow with $\hat{u}$ equal to 2% of the jet exit velocity unless there is a forward flight velocity. This small external flow is necessary to maintain a stable downstream marching solution. Previous experience[15,24] indicates that the introduction of such a small outside flow only leads to a small error in the calculated mean flow. This error does not materially affect the intensity and directivity of the radiated sound.

C. Numerical Stability Analysis

The numerical stability requirement is most stringent in the region outside the jet where there is a small artificially added mean flow velocity. In this region k and ε are zero. Hence ν_t and the stresses terms are zero. The linearized perturbation equations (6–9) are, where subscript 0 denotes mean flow variables outside the jet,

$$\frac{\partial \hat{u}'}{\partial \xi} = 0 \quad (16)$$

$$\frac{\partial \hat{v}'}{\partial \xi} = \frac{1}{u_0}\left[-\frac{1}{\rho_0\cos\alpha}\frac{\partial p'}{\partial \eta}\right] \quad (17)$$

$$\frac{\partial T'}{\partial \xi} = \frac{1}{u_0}\left[-\gamma(\gamma - 1)M_{\text{ref}}^2\frac{p_0}{\rho_0}\left(\frac{1}{\cos\alpha}\frac{\partial \hat{v}'}{\partial \eta} + \frac{1}{r}\hat{v}'\cos\alpha\right)\right] \quad (18)$$

$$\frac{\partial p'}{\partial \xi} = \frac{1}{u_0}\left[u_0\frac{p_0}{T_0}\frac{\partial T'}{\partial \xi} - p_0\left(\frac{1}{\cos\alpha}\frac{\partial \hat{v}'}{\partial \eta} + \frac{1}{r}\hat{v}'\cos\alpha\right)\right] \quad (19)$$

When $(\partial T')/(\partial \xi)$ is eliminated, it is found that

$$\frac{\partial}{\partial \xi}\begin{bmatrix}\hat{v}' \\ p\end{bmatrix} + \frac{\partial}{\partial \eta}\begin{bmatrix}p'/(\rho_0 u_0\cos\alpha) \\ \gamma p_0\hat{v}'/(u_0\cos\alpha)\end{bmatrix} + \begin{bmatrix}0 \\ \hat{v}'\gamma p_0\cos\alpha/(ru_0)\end{bmatrix} = 0 \quad (20)$$

Let us temporarily neglect the last term of Eq. (20). We will consider its presence later. For stability analysis, there is no loss of generality by considering wavelike perturbations of the form

$$\begin{bmatrix}\hat{v}' \\ p'\end{bmatrix} = \begin{bmatrix}\tilde{v} \\ \tilde{p}\end{bmatrix}e^{i(\beta\eta - \omega\xi)} \quad (21)$$

Substituting Eq. (21) into Eq. (20) and setting the determinant of the coefficient matrix of the homogeneous system to zero, it is straightforward to find that the dispersion relation of the perturbation wave solution is given by

$$\omega^2 = \beta^2\big/M_0^2\cos^2\alpha \qquad \text{or} \qquad \omega = \pm\beta/M_0\cos\alpha \quad (22)$$

where M_0 is the Mach number of the artificial ambient flow.

In this work, the computations are carried out by the dispersion-relation-preserving (DRP) scheme.[25] One of the characteristics of the DRP scheme is that the dispersion relation of the discretized system is formally the same as that of the original partial differential equations. Thus, if $\bar{\omega}(\omega)$ is the angular frequency and $\bar{\beta}(\beta)$ the wave number of the discretized DRP finite difference equations, the dispersion relation is

$$\bar{\omega}(\omega) = \pm\frac{\bar{\beta}(\beta)}{M_0\cos\alpha} \quad (23)$$

With use of the four-level optimized multistep marching DRP algorithm, it was proved in Ref. 25 that a stable and accurate numerical

solution is assured if $|\bar{\omega}\Delta\xi| \leq 0.2$. That is, by means of relation (23)

$$|\bar{\omega}\Delta\xi| = \left|\frac{\bar{\beta}\Delta\eta}{M_0\cos\alpha}\right|\frac{\Delta\xi}{\Delta\eta} \leq 0.2$$

so that

$$\Delta\xi \leq \frac{0.2 M_0\cos\alpha}{(\bar{\beta}\Delta\eta)_{\max}}\Delta\eta \qquad (24)$$

Formula (24) gives the maximum size of the marching step, $\Delta\xi$, for a stable and accurate solution. If the last term of Eq. (20) is included, it can be shown that it adds weak instability to the solution. However, such weak instability can be eliminated by the addition of artificial selective damping that will be discussed later. When numerical values are inserted into inequality (24), it is found that $\Delta\xi \leq (\Delta\eta/600)$. In the next section, we will discuss a way to speed up the computation.

D. Mesh Design

For the marching scheme to be practical, we need to be able to increase the size of the marching step $\Delta\xi$ as the computation progresses in the downstream direction. Formula (24) suggests that if a larger and larger $\Delta\eta$ can be used, then a corresponding larger and larger $\Delta\xi$ may be used. The choice of $\Delta\eta$ is dictated by the resolution requirement in computing the jet shear layer. Note that the thickness of the shear layer increases downstream. Thus, the resolution needed downstream is relaxed. In other words, as the shear layer thickness doubles, the size $\Delta\eta$ used may also be doubled. This in turn allows us to double the marching step $\Delta\xi$. To make use of this strategy, a multisize mesh in the η direction is adopted.

Figure 4 shows a multisize-mesh design that allows us to double the mesh size in the η direction whenever such a move meets the required resolution in the shear layer. In this design, the finest mesh with size Δ is used in the region extending from the wall to a point outside the shear layer of the jet. In Fig. 4, the center of the shear layer is located at a distance $(h + b)$ from the wall, where h is the initial radius of the potential core of the jet and b is the half-width of the shear layer. Let there be $(N_0 + N_1)$ mesh spacings in this region. Adjacent to this fine-mesh region is a mesh layer with mesh size equal to 2Δ. Outside the layer with mesh size 2Δ is a layer of 4Δ mesh. Outside the 4Δ mesh is a layer of 8Δ mesh and so on. Each outside layer has a mesh size equal to twice that of the adjacent inner layer.

Now as the computation proceeds downstream, it would reach a point at which the shear layer thickness b is twice that of the initial thickness. At the next step in ξ, we may remove every other mesh line in the wall region. This doubles the mesh size but retains the same spatial resolution as at the beginning of the computation. After doubling the mesh size in the η direction, this layer merges with the mesh layer immediately outside. The marching may resume using a marching step size of $2\Delta\xi$. This procedure can be repeated again and again until the desired downstream location is reached.
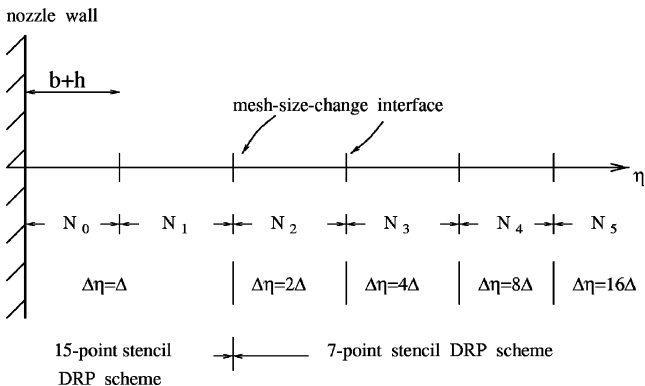

Fig. 4   Mesh design for downstream marching algorithm.

To implement the algorithm, special finite difference stencils are needed at the mesh-size change interface. Such stencils have been formulated and analyzed by Tam and Kurbatskii[26] in their development of a multi-size-mesh multi-time-step DRP scheme. What remains to be decided in the marching scheme is the distribution of the number of mesh points $N_0, N_1, N_2, \ldots$. The choice of $N_0, N_1, N_2, \ldots$, turns out to be fairly important. They are crucial to the stability of the computation. As indicated in Fig. 4, the η derivatives of the governing equations are to be approximated by a 15-point stencil DRP scheme[27] in the innermost mesh layer. For all of the outer mesh layers, the use of a 7-point stencil DRP scheme will suffice.

Because, as mentioned before, the marching scheme is mildly unstable, grid-to-grid oscillations are generated within the shear layer where the velocity gradient is large. These spurious short waves propagate through the shear layer until they are outside the shear layer. They propagate at a high speed in the ambient region where $M_0 \cong 0.02$. On reaching the first interface where there is a change in mesh size, they are reflected back with a considerable increase in amplitude. When the reflected waves propagate back to the center of the shear layer, they are again reflected back. In a sense, the spurious waves are trapped between the shear layer and the first mesh-size change interface. Each reflection results in higher wave amplitude. Eventually, this could cause the numerical solution to blow up.

To render the numerical solution stable, it is necessary to add artificial selective damping[28] so that the grid-to-grid oscillations are practically damped after propagating from the shear layer to the first mesh-size change interface. When the artificial selective damping is added, the dispersion relation of the discretized equations, instead of given by solution (22), now becomes

$$\bar{\omega} = \pm(\bar{\beta}/M_0\cos\alpha) - i[D(\beta\Delta\eta)/Re_\Delta\Delta\eta] \qquad (25)$$

where Re_Δ is the mesh Reynolds number and $D(\beta\Delta\eta)$ is the damping function.[28] The speed of propagation is given by the group velocity, which can be estimated by using Eq. (25) without the damping term. By differentiating Eq. (25) with respect to β and on taking $(d\bar{\omega})/(d\omega) \cong 1.0$ (small $\Delta\xi$ steps), we find

$$\frac{d\omega}{d\beta} = \frac{1}{M_0\cos\alpha}\frac{d\bar{\beta}}{d\beta} \qquad (26)$$

The total damping factor for spurious grid-to-grid oscillations propagating from the shear layer to the first mesh-size change interface, a distance of $N_1\Delta\eta$ (Fig. 4), is, therefore, given by

$$\exp\left\{-\frac{D(\beta\Delta\eta)}{Re_\Delta\Delta\eta}\frac{N_1\Delta\eta}{[(1/M_0\cos\alpha)(d\bar{\beta}/d\beta)]}\right\} \qquad (27)$$

To ensure that the spurious waves are heavily damped but at the same time, without materially damping the physical solution (the long waves), we will use a 15-point optimized damping stencil. (The coefficients of the damping stencil are provided in the Appendix.) The wave number for grid-to-grid oscillation corresponds to $\beta\Delta\eta = \pi$. We noted that $D(\pi) = 1.0$ and $(d\bar{\beta})/(d\beta)|_{\beta=\pi} = 5.0$ for the 15-point stencil DRP scheme. By inserting these values into exponent (27) and requiring a damping factor of $e^{-5}(=0.007)$, we find

$$(1/Re_\Delta)(M_0\cos\alpha N_1/5) = 5$$

When $M_0 = 0.02$, $\alpha = 20$ deg, and $Re_\Delta^{-1} = 7.82$ is used, it is easy to find $N_1 \geq 170$. Therefore, to maintain sufficient distance between the shear layer and the first mesh-size change interface after each doubling of the mesh size Δ in the innermost mesh layer, we set $N_1 = 170$ and $N_j \cong 110$, $j = 2, 3, 4, \ldots$.

The main purpose of adding artificial selective damping is to remove spurious waves from the computation so as to maintain accuracy and stability. However, artificial selective damping may also cause slight damping to the physical solution with wavelength $\beta\Delta\eta \leq 1.0$. It is straightforward to show, with $D(1.0) \cong 2 \times 10^{-5}$ for the 15-point damping stencil, that the damping is quite negligible.

E. Wall and Outgoing Wave Boundary Conditions

As shown in Fig. 2, the jet mean flow solution is to be computed by marching the solution starting at the left boundary of region 1 to the right boundary and then starting at the left boundary of region 2 and marching the solution to the right boundary. To complete the marching scheme, we need to impose a wall boundary condition at the nozzle wall and an outgoing wave boundary condition at the upper boundary of the computation domain. In this work, a no-penetration boundary condition is enforced at the wall. This is implemented by adopting the ghost point method of Tam and Dong.[29]

For large η, Eqs. (16–19) are the linearized perturbation equations of the governing RANS equations. The solution of Eq. (16) is $\hat{u}' = 0$. Thus, the appropriate boundary condition for $\hat{u}$ is $\hat{u} = u_0$. For large r, the asymptotic solution of Eq. (20), which represents outgoing waves, has the form

$$p' = F\left(\eta + r_0 - \xi/M_0 \cos\alpha\right)/r^{\frac{1}{2}} + \cdots \qquad (28)$$

Both $\hat{v}'$ and T' have a similar form. When the unknown functions are eliminated by differentiation and addition, it is straightforward to find that an appropriate set of outgoing wave boundary conditions for small α is

$$\hat{u} = u_0, \qquad M_0 \cos\alpha \frac{\partial}{\partial\xi}\begin{bmatrix} \hat{v} \\ p \\ T \end{bmatrix} + \frac{\partial}{\partial\eta}\begin{bmatrix} \hat{v} \\ p \\ T \end{bmatrix} + \frac{1}{2r}\begin{bmatrix} \hat{v} \\ p - p_0 \\ T - T_0 \end{bmatrix} = 0 \qquad (29)$$

F. Plug Nozzle with Blunt Nose

Downstream of the blunt nose of an external plug nozzle, the flow reverses to form a recirculation region as shown in Fig. 5a. Parabolized computation cannot be used to calculate reverse flow because information is transmitted upstream. For noise prediction purposes, this region is not of significance. We will approximate the recirculation region by an almost stagnant region. It will be assumed that there is a weak outflow from the blunt end of the nozzle as shown in Fig. 5b. The flow moves slowly downstream and is then entrained by the flow of the primary jet.

We switch to a cylindrical coordinate system with the x axis coinciding with the jet centerline right downstream of the plug nozzle. To continue the parabolized solution farther downstream, we need starting profiles for the flow variables. Let H be the radius of the blunt nose of the plug nozzle. For $r \geq H$, the u and v velocity profiles are given by the parabolized solution computed from upstream. Suppose the u-velocity component at $r = H$ is u_H (Fig. 6a). In the region $r < H$, we propose to use the following nearly stagnant flow
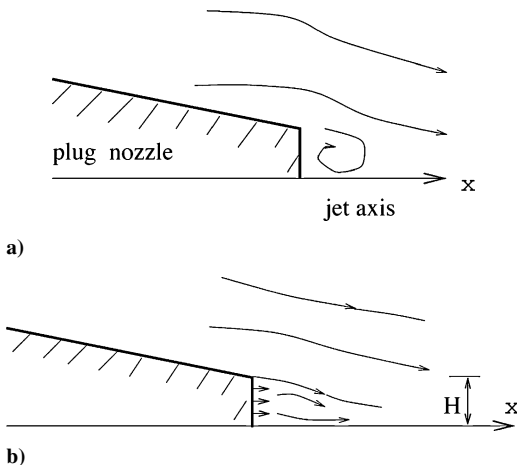

Fig. 5 Flow model downstream of blunt nose of plug nozzle: a) recirculation flow and b) nearly stagnant flow model.
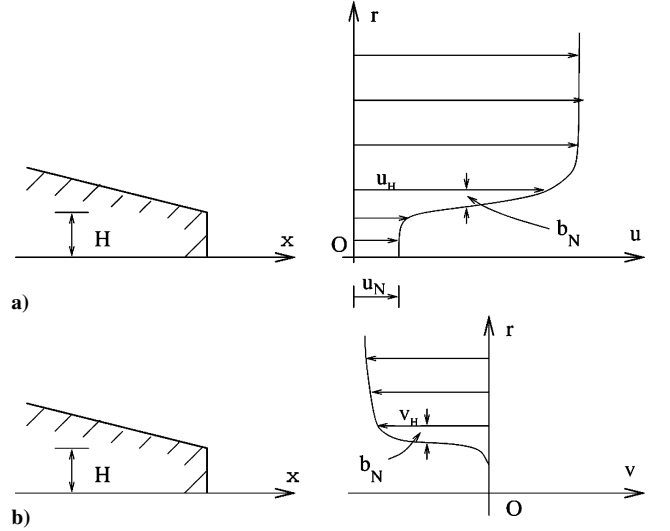

Fig. 6 Starting profiles for velocity components downstream of blunt nose of a plug nozzle: a) u component and b) v component.

model as the starting velocity profile for u:

$$u = \begin{cases} u \text{ as calculated by the parabolized} & r \geq H \\ \quad \text{solution from upstream,} & \\ (u_H - u_N)\exp\left\{-(\ell_n 2)[(H-r)/b_N]^2\right\} + u_N, & r < H \end{cases} \qquad (30)$$

where $u_N = 2\%$ of the velocity of secondary jet at nozzle exit, $b_N = 0.1H$, and u_H is u at $r = H$.

Because of the plug nozzle geometry, v_H (the radial velocity component at $r = H$) is negative. For $r < H$, we propose to use the following starting profile for the v-velocity component (Fig. 6b)

$$v = v_H \exp\left\{-(\ell_n 2)[(H-r)/b_N]^2\right\} \qquad (31)$$

Because the flow is assumed to be nearly stagnant immediately downstream of the blunt nose of the plug nozzle, we will let the starting values of p and T to be constants. Thus,

$$p = p_H, \qquad T = T_H, \qquad r \leq H \qquad (32)$$

where p_H and T_H are the values at $r = H$ of the parabolized solution computed from upstream.

III. Comparison Between Computed and Measured Mean Velocity Profile

Mean flow data of dual-stream jets from separate flow nozzles are not readily available in the literature. However, recently a set of high-quality total pressure and total temperature data, as well as a companion set of jet noise data, were measured by Thomas and Kinzie[30] as a part of NASA jet noise data acquisition effort. The data sets have not been published but they are made available to the present investigation. When it is assumed that the static pressure inside the jet is equal to ambient pressure (boundary-layer argument), it is possible to convert these data to mean velocity profiles. Let p_{total} be T_{total} the measured total pressure and temperature and p_∞ be the ambient pressure; it is straightforward to derive the following formula for the velocity u of the jet in terms of the measured data:

$$u^2 = \frac{2RT_{\text{total}}(p_{\text{total}}/p_\infty - 1)}{1 + [(\gamma-1)/\gamma](p_{\text{total}}/p_\infty - 1)}$$

where R is the gas constant and γ is the ratio of specific heats.

Figure 7 shows comparisons of the calculated and measured mean flow velocity profiles of a bypass ratio 8 dual-stream jet inside an open wind tunnel at Mach number 0.28. The primary jet Mach number and temperature ratio are 0.69 and 2.82, respectively. The secondary jet Mach number and total temperature ratio are 0.8 and 1.2, respectively. Figures 7a–7d show profiles at $x/D_p = 2.5, 5.0, 10.0$,
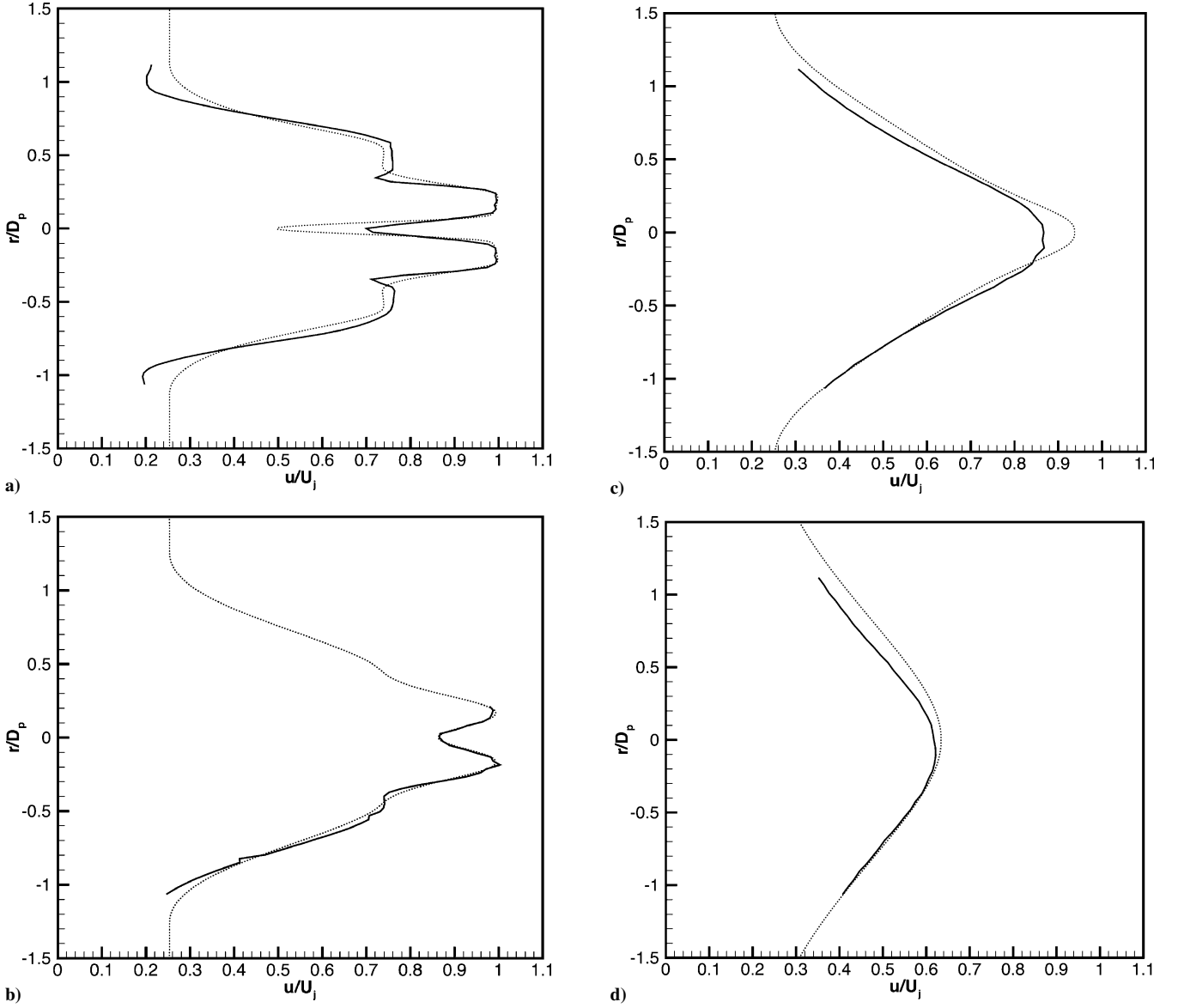
Fig. 7   Comparisons of measured and calculated velocity profiles of jet mean flow, $M_p = 0.69$, $T_p/T_a = 2.82$, $M_s = 0.8$, $T_s/T_a = 1.2$, bypass ratio 8, wind-tunnel Mach number 0.28: ——, measured and ····, computed; a) $x/D_p = 2.5$, b) $x/D_p = 5.0$, c) $x/D_p = 10.0$, and d) $x/D_p = 17.0$ (data from Ref. 30).

and 17.0, where D_p is the diameter of the primary jet. The measured data indicate a slight drift of the jet centerline in the downstream direction. Figure 8 shows similar comparisons for a bypass ratio 5 dual-stream jet. The primary jet Mach number and temperature ratio are 0.77 and 2.81, respectively. The secondary jet Mach number and total temperature ratio are 0.86 and 1.2, respectively. The velocity profiles at $x/D_p = 2.0, 5.0, 10.0,$ and 17.0 are shown in Figs. 8a–8d. Overall, the computed velocity profiles for both bypass ratio jets are in good agreement with experimental data.

IV.   Computation of Noise from Fine-Scale Turbulence

Once the mean flow and the κ and ε values are computed by the parabolized algorithm described in Sec. II, the fine-scale turbulence noise from the jet may be calculated by the extended Tam and Auriault theory[12] (also see Ref. 17). The far-field noise spectrum, $S[R, \Theta, \phi, (f D_j/u_j)]$, at a point with polar coordinates (R, Θ, ϕ) with respect to a polar coordinate system centered at the exit plane of the primary nozzle is given by

$$S\left(R, \Theta, \phi, \frac{f D_j}{u_j}\right) = 10 \log\left[\frac{4\pi S(\boldsymbol{x}, \omega)}{p_{\text{ref}}^2 (D_j/u_j)}\right] \qquad (33)$$

where

$$S(\boldsymbol{x}, \omega) = \frac{4\pi^3}{(\ln 2)^{\frac{3}{2}}} \iiint_{v_{\text{jet}}} \frac{\Gamma\left(v + \frac{1}{2}\right)}{\Gamma(v)} \left(\frac{\hat{q}_s^2}{c^2}\right) \frac{\ell_s^3}{\tau_s}$$

$$\times \frac{|p_a(\boldsymbol{x}_2, \boldsymbol{x}, \omega)|^2 \exp\left[-\omega^2 \ell_s^2 / \bar{u}^2 4(\ln 2)\right]}{\left\{1 + \omega^2 \tau_s^2 [1 - (\bar{u}/a_\infty) \cos \Theta]^2\right\}^{v + \frac{1}{2}}} \, d\boldsymbol{x}_2 \qquad (34)$$

For convenience, we will use subscript p to denote variables associated with the primary jet and subscript s to denote variables associated with the secondary jet. For example, D_p and D_s are the nozzle exit diameters of the primary and secondary jet, u_p and u_s are the fully expanded velocities of the primary and secondary jet. In Eq. (34), $p_a(\boldsymbol{x}_2, \boldsymbol{x}, \omega)$ is the adjoint Green's function and $\omega = 2\pi f$ is the angular frequency. In this study, the locally parallel flow approximation is adopted in computing the adjoint Green's function as in Refs. 12–14 and 17. At the nozzle wall, the boundary condition for the adjoint Green's function, derived by Tam and Auriault,[31] is $\boldsymbol{v}^{(a)} \cdot \hat{\boldsymbol{n}} = \boldsymbol{0}$, where $\hat{\boldsymbol{n}}$ is the unit normal of the solid surface and $\boldsymbol{v}^{(a)}$ is the adjoint acoustic velocity. The quantities $(\hat{q}_s^2)/(c^2)$, v, ℓ_s, and
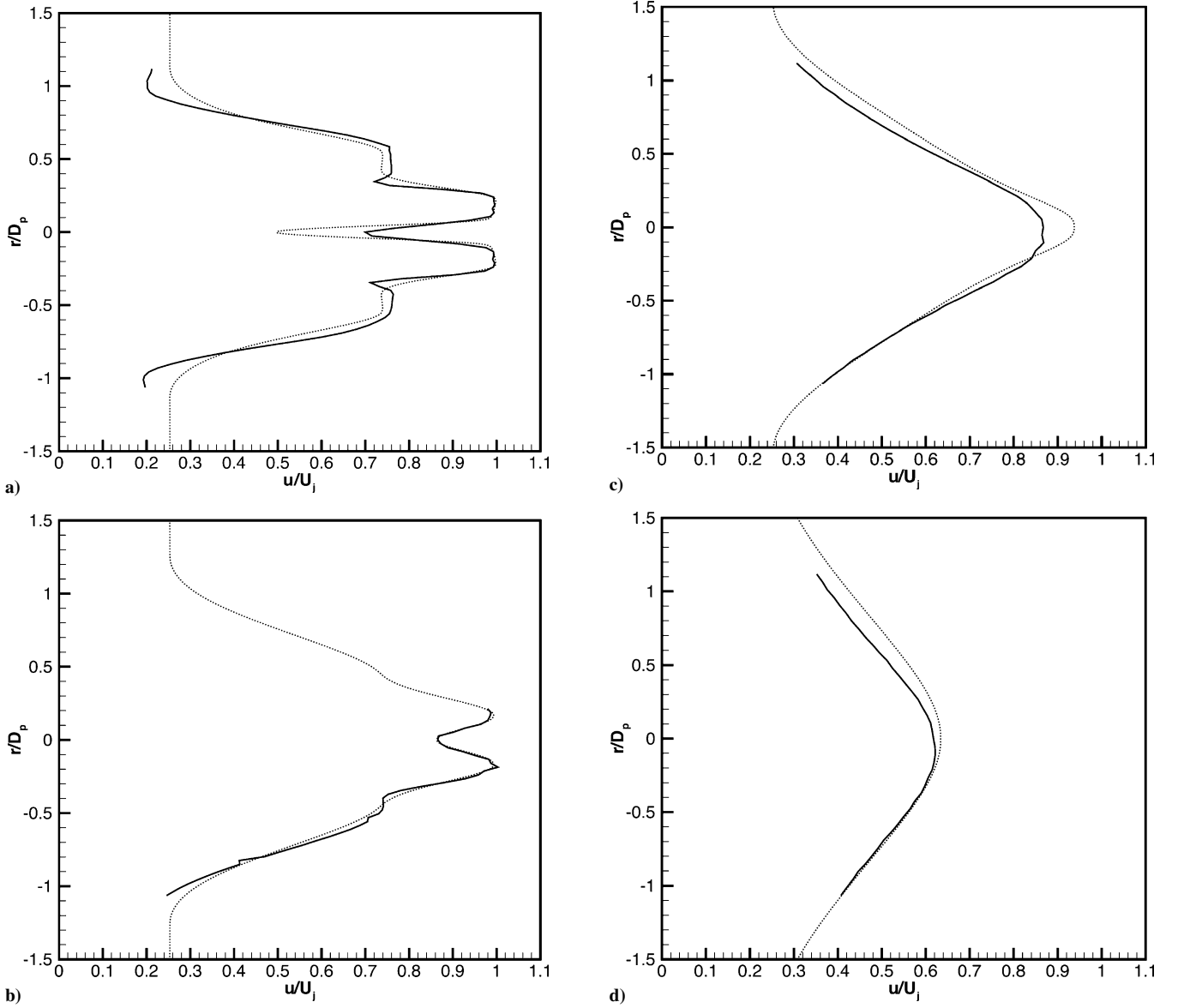
Fig. 8 Comparisons of measured and calculated velocity profiles of jet mean flow, $M_p = 0.77$, $T_p/T_a = 2.81$, $M_s = 0.86$, $T_s/T_a = 1.2$, bypass ratio 5, wind-tunnel Mach number 0.28: ——, measured and · · · ·, computed; a) $x/D_p = 2.5$, b) $x/D_p = 5.0$, c) $x/D_p = 10.0$, and d) $x/D_p = 17.0$.

τ_s are related to k and ε of the k–ε turbulence model as follows:

$$\nu = \frac{1}{2} + \begin{cases} c_\eta \dfrac{k^{\frac{3}{2}}}{\varepsilon} \dfrac{1}{\rho} \left| \dfrac{\mathrm{d}\rho}{\mathrm{d}r} \right| & (35a) \\[2ex] 0 & (35b) \end{cases}$$

$$\frac{\hat{q}_s^2}{c^2} = A^2 q^2 + \begin{cases} B \dfrac{k^{\frac{3}{2}}}{\varepsilon} \dfrac{1}{\rho} \left| \dfrac{\mathrm{d}\rho}{\mathrm{d}r} \right| q^2 & (36a) \\[2ex] 0 & (36b) \end{cases}$$

$$\ell_s = c_\ell \frac{k^{\frac{3}{2}}}{\varepsilon} + \begin{cases} c_{\ell\rho} \dfrac{k^3}{\varepsilon^2} \dfrac{1}{\rho} \left| \dfrac{\mathrm{d}\rho}{\mathrm{d}r} \right| & (37a) \\[2ex] 0 & (37b) \end{cases}$$

$$\tau_s = c_\tau \frac{k}{\varepsilon} + \begin{cases} c_{\tau\rho} \dfrac{k^{\frac{5}{2}}}{\varepsilon^2} \dfrac{1}{\rho} \left| \dfrac{\mathrm{d}\rho}{\mathrm{d}r} \right| & (38a) \\[2ex] 0 & (38b) \end{cases}$$

In Eqs. (35–38), formulas (35a–38a) are to be used when $(\mathrm{d}u)/(\mathrm{d}r)$ and $(\mathrm{d}p)/(\mathrm{d}r)$ have opposite signs. Formulas (35b–38b) are used when they have the same sign. The three constants A, c_ℓ, and c_τ were determined empirically by Tam and Auriault,[12] and they were assigned the values

$$A = 0.755, \qquad c_\ell = 0.256, \qquad c_\tau = 0.233$$

The remaining four constants were given the values

$$c_\eta = 2.1599, \qquad B = 0.806, \qquad c_{\ell\rho} = -0.026, \qquad c_{\tau\rho} = -0.2527$$

in Ref. 17.

V. Comparisons with Experiments

We will compare the computed fine scale turbulence noise spectra with dual-stream jet noise data measured at the NASA Langley Research Center by Thomas and Kinzie[30] and at The Boeing Company by Bhat.[20] The Boeing data have not been published but are made available to this investigation by Bhat. They were measured as a part of the effort described in Ref. 20. The nozzles used in the Boeing experiments had no external plug. The nozzles used in the NASA

experiment had external plugs. A list of the dimensions of the nozzle geometry follows (Fig. 1).

Boeing nozzle configuration 2 (no external plug):

$$D_p = 2.45 \text{ in.}, \quad D_s = 6.0 \text{ in.}, \quad X = 5.0 \text{ in.}, \quad \alpha = 10.06 \text{ deg}$$

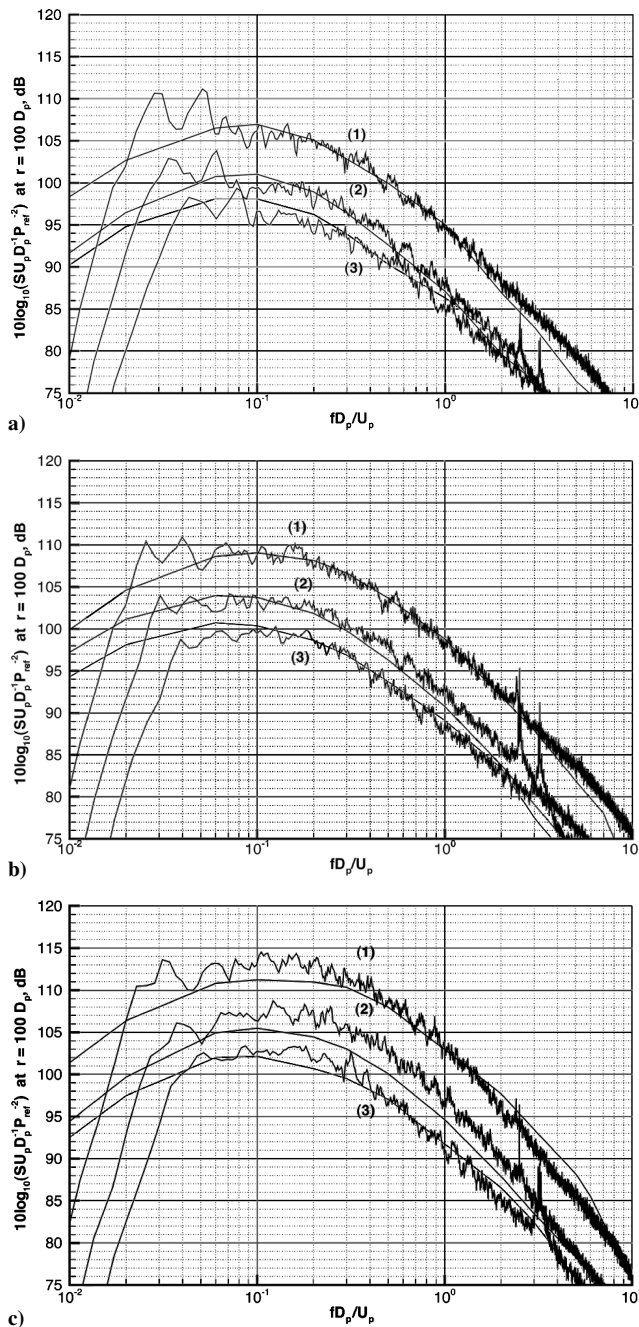$$\text{Area}_{\text{secondary exit}}/\text{Area}_{\text{primary exit}} = 3.0$$

Boeing nozzle configuration 4 (no external plug):

$$D_p = 3.46 \text{ in.}, \quad D_s = 6.0 \text{ in.}, \quad X = 5.0 \text{ in.}, \quad \alpha = 8.09 \text{ deg}$$

$$\text{Area}_{\text{secondary exit}}/\text{Area}_{\text{primary exit}} = 1.0$$

a)

b)

c)

Fig. 9 Comparisons between calculated and measured noise spectra, data from Boeing (Bhat[20]) nozzle configuration 2: 1) $M_p = 0.99$, $T_p/T_a = 2.78$, $M_s = 0.96$, and $T_s/T_a = 1.0$; 2) $M_p = 0.81$, $T_p/T_a = 2.78$, $M_s = 0.71$, and $T_s/T_a = 1.0$; and 3) $M_p = 0.62$, $T_p/T_a = 2.78$, $M_s = 0.71$, and $T_s/T_a = 1.0$; a) $\Theta = 60$ deg, b) $\Theta = 90$ deg, and c) $\Theta = 110$ deg.

NASA bypass ratio 5 nozzle with external plug:

$$D_p = 5.07 \text{ in.}, \quad D_s = 9.45 \text{ in.}, \quad X_1 = 4.25 \text{ in.}, \quad X_2 = 9.57 \text{ in.}$$

$$\alpha = 14.19 \text{ deg}, \quad \beta = 12.78 \text{ deg}$$

$$\text{Area}_{\text{secondary exit}}/\text{Area}_{\text{primary exit}} = 2.65$$

NASA bypass ratio 8 nozzle with external plug:

$$D_p = 4.79 \text{ in.}, \quad D_s = 9.45 \text{ in.}, \quad X_1 = 4.25 \text{ in.}, \quad X_2 = 9.77 \text{ in.}$$

$$\alpha = 14.19 \text{ deg}, \quad \beta = 13.27 \text{ deg}$$

$$\text{Area}_{\text{secondary exit}}/\text{Area}_{\text{primary exit}} = 4.16$$

Figure 9 shows comparisons between the computed noise spectra for nozzle configuration 2 and the Boeing data measured by Bhat.[20] (Bhat informed the authors that the low-frequency portion of the measured noise spectra had been artificially rolled down.) Data at three jet operating conditions and three directions are shown. Figure 10 shows similar comparisons for nozzle configuration 4. Data include measurements at two jet operating conditions. As can be seen from Figs. 9 and 10, there are very favorable agreements between computed noise spectra and measurements. Other cases in addition to those displayed in Figs. 9 and 10 have also been calculated. They are not included here due to space limitation. However, we would like to stress that, in each of these cases, the computed spectra are in good agreement with experiment.

Figures 11 and 12 show comparisons of calculated noise spectra with data measured at the NASA Langley Research Center by Thomas and Kinzie.[30] Figure 11 is for bypass ratio 5 jets at two operating conditions. The spectra are measured at inlet angle $\theta = 50, 70, 90$, and 110 deg. Figure 12 shows similar data for bypass ratio 8 jets. In the experiments, the jets were enclosed in an open wind tunnel at a forward-flight Mach number of 0.1. The calculated spectra also include the effect of the open wind tunnel at the same wind-tunnel Mach number. It is self-evident that the computed noise spectra are in good agreement with experimental measurements. This is true for spectrum levels and shapes as well as directivities.

It is known that forward flight can cause significant reduction in jet noise. A general rule of thumb is that for every 0.2 increase in forward flight Mach number, there is an approximately 4-dB decrease in sound pressure level. Figure 13 shows the calculated and measured noise spectra at a simulated forward flight Mach number
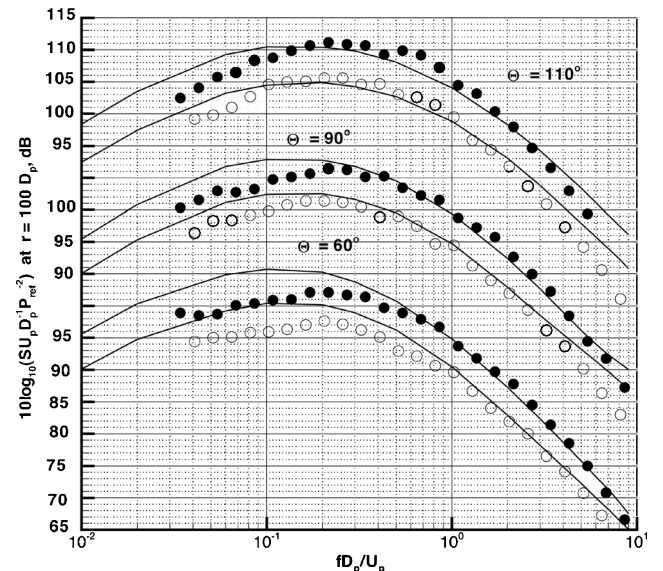

Fig. 10 Comparisons between calculated and measured noise spectra, data from Boeing (Bhat[20]) nozzle configuration 4: ●●●, $M_p = 0.99$, $T_p/T_a = 2.75$, $M_s = 0.71$, $T_s/T_a = 1.0$; and ○○○, $M_p = 0.81$, $T_p/T_a = 2.75$, $M_s = 0.71$, $T_s/T_a = 1.0$.
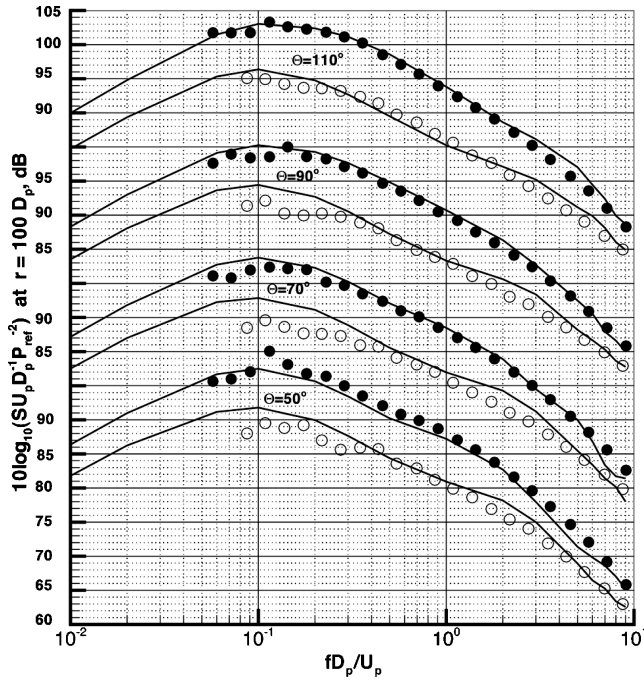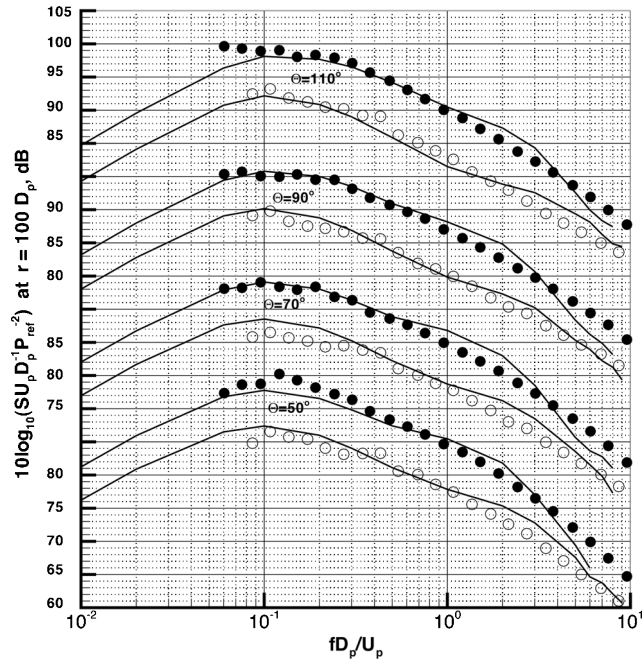
Fig. 11 Comparisons between calculated and measured noise spectra, bypass ratio 5, wind tunnel Mach number 0.1, data from Ref. 30: ●●●, $M_p = 0.77$, $T_p/T_a = 2.81$, $M_s = 0.86$, $T_s/T_a = 1.22$; **and** ○○○, $M_p = 0.55$, $T_p/T_a = 2.45$, $M_s = 0.74$, $T_s/T_a = 1.15$.

Fig. 13 Comparisons between calculated and measured noise spectra, bypass ratio 5, wind tunnel Mach number 0.28, data from Ref. 30: ○○○, $M_p = 0.77$, $T_p/T_a = 2.81$, $M_s = 0.86$, $T_s/T_a = 1.22$.

Fig. 12 Comparisons between calculated and measured noise spectra, bypass ratio 8, wind tunnel Mach number 0.1, data from Ref. 30: ●●●, $M_p = 0.74$, $T_p/T_a = 2.45$, $M_s = 0.8$, $T_s/T_a = 1.2$; **and** ○○○, $M_p = 0.51$, $T_p/T_a = 2.49$, $M_s = 0.66$, $T_s/T_a = 1.2$.

Fig. 14 Comparisons between calculated and measured noise spectra, bypass ratio 8, wind tunnel Mach number 0.28, data from Ref. 30: ○○○, $M_p = 0.74$, $T_p/T_a = 2.45$, $M_s = 0.8$, $T_s/T_a = 1.2$.

0.28 for a dual-stream jet at bypass ratio 5. When the spectra are compared with those of Fig. 11, it is clear that there is, indeed, a noise reduction of about 4 dB. Figure 14 shows similar comparisons at bypass ratio 8. Again good agreements are obtained between predictions and measurements in both cases.

In addition to predicting the far-field noise, the Tam and Auriault theory[12] can also calculate the noise source distribution inside the jet plume. In a recent work, Tam et al.[32] demonstrated that the theoretical predictions of the noise source distribution in supersonic jets of Mach number 1.47, 1.97, and 2.47 were in good agreement with
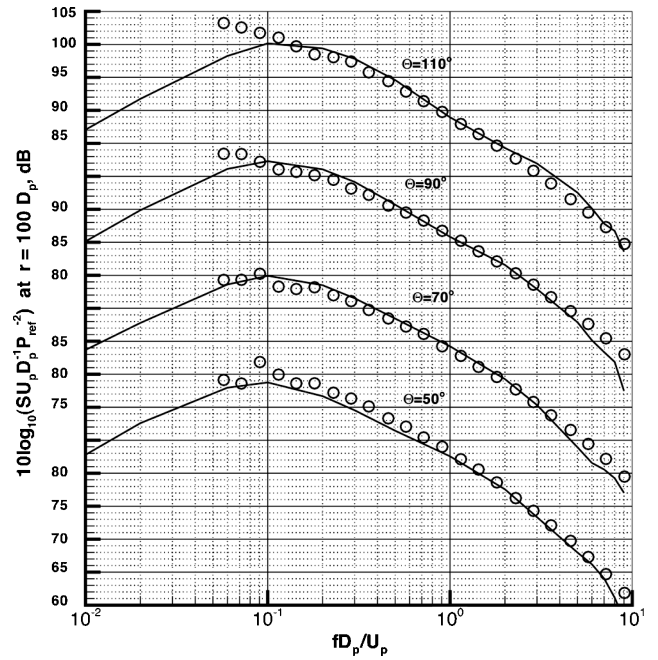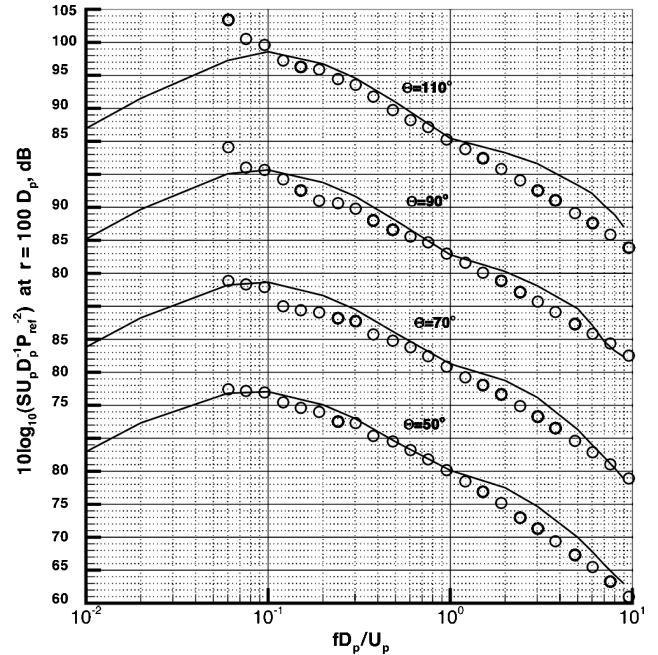
the experimental measurements of Schlinker[33] and Laufer et al.[34] This is true for both noise intensity (integrated over all frequencies) as well as at selected Strouhal numbers. For a dual-stream jet, the shear layer between the secondary jet and the ambient gas (region 1 of Fig. 15), the shear layer between the primary and the secondary jet (region 2), the fully developed jet (region 3), and the wake downstream of the plug nozzle (region 4) are plausible noise sources of the jet. To assess the relative importance of these noise sources, the noise radiated in the $\theta = 90$ deg direction from the four regions are calculated. Figure 16 shows the noise spectrum from each of the four regions as well as the total noise spectrum for a bypass ratio 5 jet. It is readily seen from Fig. 16 that the fully developed jet (region 3) produces almost all of the low-frequency noise of the
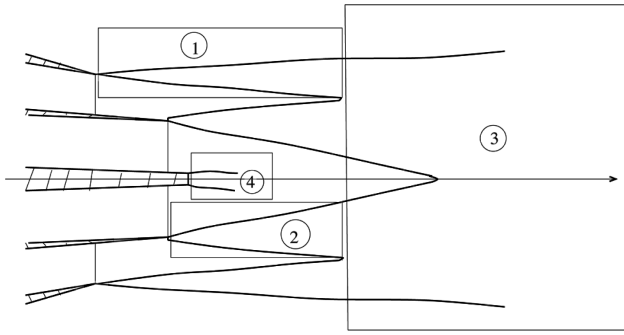
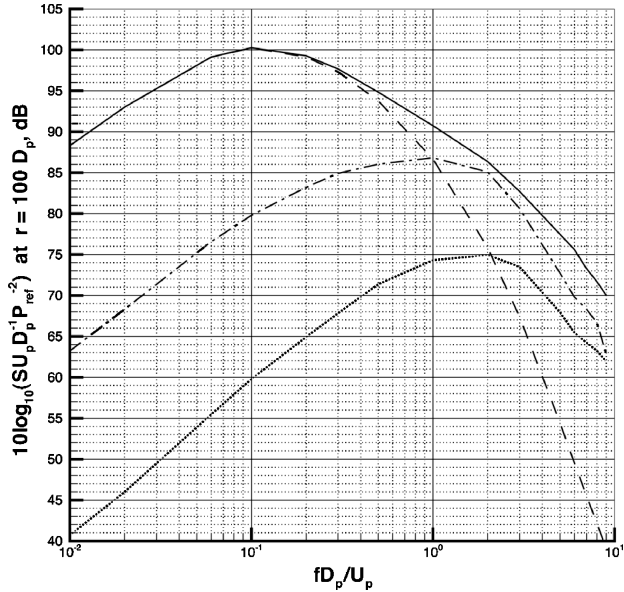**Fig. 15 Four noise source regions of dual-stream jet from separated flow nozzle with external plug.**

Fig. 16 Contributions to noise spectrum of bypass ratio 5 jet with wind-tunnel Mach number 0.1, at $\Theta = 90$ deg from various source regions: $\circ\circ\circ$, $M_p = 0.77$, $T_p/T_a = 2.81$, $M_s = 0.86$, $T_s/T_a = 1.2$: ——, noise spectrum of the entire jet; —·—, noise from region 1; ●●●, noise from region 2; and – – –, noise from region 3.
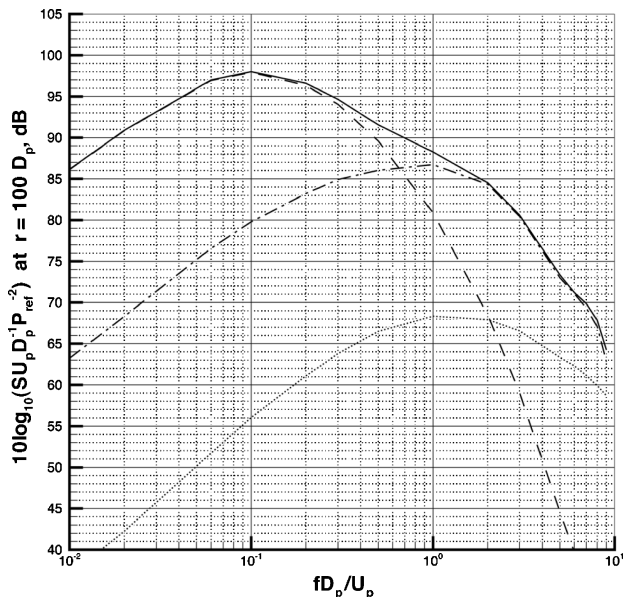

Fig. 17 Contributions to noise spectrum of bypass ratio 8 jet with wind tunnel Mach number 0.1, at $\Theta = 90$ deg from various source regions; $M_p = 0.77$, $T_p/T_a = 2.81$, $M_s = 0.86$, and $T_s/T_a = 1.2$: ——, noise spectrum of the entire jet; —·—, noise from region 1; ●●●, noise from region 2; and – – –, noise from region 3.

jet. The shear layer between the secondary jet and the ambient gas (region 1) is responsible for most of the high-frequency jet noise. Region 2 contributes only a small fraction of high-frequency noise. Region 4 is an unimportant source of jet noise. Figure 17 is a similar plot for a bypass ratio 8 jet. The conclusion is the same. Thus, for noise suppression purposes, attention should be concentrated on the turbulence in the fully developed region of the jet, as well as the outer shear layer of the secondary jet.

VI. Conclusions

In this work, a method to compute the mean flows of dual-stream jets from separate flow nozzles is provided. This method uses the parabolized RANS equations with the modified k–ε turbulence model. The method is stable and efficient. Computed results are in good agreement with experimental measurements.

The Tam and Auriault fine-scale jet turbulence noise theory[12] as extended by Tam et al.[17] is used to calculate the noise from dual-stream jets. In all of the computations, the same empirical constants established in Refs. 12 and 17 for single-stream jets are used. Comparisons with noise spectra measured at Boeing by Bhat[20] and at NASA Langley Research Center by Thomas and Kinzie[30] are made. The Boeing data are from nozzles without an external center plug. The NASA data are from nozzles with an external plug at bypass ratios of 5 and 8. Good agreements are found in all cases.

In developing their fine-scale turbulence noise theory of high-speed jets, Tam and Auriault[12] used exclusively data from single-stream round jets. However, as already mentioned, the theory was found to provide good predictions for nonaxisymmetric jet noise[13] as well as noise from jets in simulated forward flight.[14] In the present investigation, the theory is applied to dual-stream jets from separate flow nozzles with and without an external center plug. This application involves flow configurations that are beyond the database of the original formulation. We believe this offers a critical test of the validity and accuracy of the theory for more general applications. The good agreements found in all of the test cases for dual-stream jets may be considered as providing confidence in the use of the semi-empirical theory for routine engineering predictions and designs.

Appendix: Coefficients of 15-Point Damping Stencil

The coefficients are

$$d(0) = 0.2042241813072920$$
$$d(1) = d(-1) = -0.1799016298200503$$
$$d(2) = d(-2) = 0.1224349282118140$$
$$d(3) = d(-3) = -6.3456279827554890E-02$$
$$d(4) = d(-4) = 2.4341225689340974E-02$$
$$d(5) = d(-5) = -6.5519987489327603E-03$$
$$d(6) = d(-6) = 1.1117554451990776E-03$$
$$d(7) = d(-7) = -9.0091603462069583E-05$$

Acknowledgments

References

[1]Crow, S. C., and Champagne, F. H., "Orderly Structures in Jet Turbulence," *Journal of Fluid Mechanics*, Vol. 48, 1971, pp. 547–591.

[2]Brown, G. L., and Roshko, A., "On Density Effects and Large Structures in Turbulent Mixing Layers," *Journal of Fluid Mechanics*, Vol. 64, 1974, pp. 775–816.

[3]Tam, C. K. W., Golebiowski, M., and Seiner, J. M., "Two Components of Turbulent Mixing Noise from Supersonic Jets," AIAA Paper 96-1716, May 1996.

[4]Tam, C. K. W., "Jet Noise: Since 1952," *Theoretical and Computational Fluid Dynamics*, Vol. 10, No. 10, 1998, pp. 393–405.

[5]Tam, C. K. W., and Zaman, K. B. M. Q., "Subsonic Jet Noise from Nonaxisymmetric and Tabbed Nozzles," *AIAA Journal*, Vol. 38, No. 4, 2000, pp. 592–599.

[6]Viswanathan, K., "Analysis of the Two Similarity Components of Turbulent Mixing Noise," *AIAA Journal*, Vol. 40, No. 9, 2002, pp. 1734–1744.

[7]Panda, J., and Seasholtz, R. G., "Experimental Investigation of Density Fluctuations in High-Speed Jets and Correlation with Generated Noise," *Journal of Fluid Mechanics*, Vol. 450, 2002, pp. 97–130.

[8]Panda, J., Seasholtz, R. G., and Elam, K. A., "Further Progress in Noise Source Identification in High-Speed Jets via Causality Principle," AIAA Paper 2003-3126, May 2003.

[9]Hurdle, P. M., Meecham, W. C., and Hodder, B. K., "Investigation of the Aerodynamic Noise Generating Region of a Jet Engine by Means of the Simple Source Fluid Dilatation Model," *Journal of the Acoustical Society of America*, Vol. 56, No. 6, 1974, pp. 1708–1721.

[10]Schaffar, M., "Direct Measurements of the Correlation Between Axial in-Jet Velocity Fluctuations and Far Field Noise near the Axis of a Cold Jet," *Journal of Sound and Vibration*, Vol. 64, No. 1, 1979, pp. 73–83.

[11]Bogey, C., and Bailly, C., "Investigation of Sound Sources in Subsonic Jets Using Causality Methods on LES data," AIAA Paper 2005-2885, May 2005.

[12]Tam, C. K. W., and Auriault, L., "Jet Mixing Noise from Fine Scale Turbulence," *AIAA Journal*, Vol. 37, No. 2, 1999, pp. 145–153.

[13]Tam, C. K. W., and Pastouchenko, N. N., "Noise from Fine Scale Turbulence of Nonaxisymmetric Jets," *AIAA Journal*, Vol. 40, No. 2, 2002, pp. 456–464.

[14]Tam, C. K. W., Pastouchenko, N., and Auriault, L., "Effects of Forward Flight on Jet Mixing Noise from Fine-Scale Turbulence," *AIAA Journal*, Vol. 39, No. 7, 2001, pp. 1261–1269.

[15]Tam, C. K. W., and Ganesan, A., "Modified k–ε Turbulence Model for Calculating Hot Jet Mean Flows and Noise," *AIAA Journal*, Vol. 42, No. 1, 2004, pp. 26–34.

[16]Doty, M. J., and McLaughlin, D. K., "Two-Point Correlations of Density Gradient Fluctuations in High Speed Jets Using Optical Deflectometry," AIAA Paper 2002-0367, Jan. 2002.

[17]Tam, C. K. W., Pastouchenko, N. N., and Viswanathan, K., "Fine Scale Turbulence Noise from Hot Jets," *AIAA Journal*, Vol. 43, No. 8, 2005, pp. 1675–1683.

[18]Georgiadis, N. J., and Papamoschou, D., "Computational Investigations of High-Speed Dual-Stream Jets," AIAA Paper 2003-3311, May 2003.

[19]Birch, S. F., Lyubimov, D. A., Secundov, A. N., and Yakubovsky, K. Y., "Numerical Modeling Requirements for Coaxial and Chevron Nozzle Flows," AIAA Paper 2003-3287, May 2003.

[20]Bhat, T. R. S., "Experimental Study of Acoustic Characteristics of Jets from Dual Flow Nozzles," AIAA Paper 2001-2183, May 2001.

[21]Nesbitt, E., Elkoby, R., Bhat, T. R. S., Strange, P. J. R., and Mead, C. J., "Correlating Model-Scale Test Results of Dual Flow Nozzle Jets," AIAA Paper 2002-2487, June 2002.

[22]Mead, C. J., and Strange, P. J. R., "Under-Wing Installation Effects on Jet Noise at Sideline," AIAA Paper 98-2207, June 1998.

[23]Blackner, A. M., and Bhat, T. R. S., "Installation Effects on Coaxial Jet Noise—An Experimental Study," AIAA Paper 98-0080, Jan. 1998.

[24]Thies, A. T., and Tam, C. K. W., "Computation of Turbulent Axisymmetric and Nonaxisymmetric Jet Flows Using the k–ε Model," *AIAA Journal*, Vol. 34, No. 2, 1996, pp. 309–316.

[25]Tam, C. K. W., and Webb, J. C., "Dispersion-Relation-Preserving Finite Difference Scheme for Computational Acoustics," *Journal of Computational Physics*, Vol. 107, No. 2, 1993, pp. 262–281.

[26]Tam, C. K. W., and Kurbatskii, K. A., "Multi-Size-Mesh Multi-Time-Step Dispersion-Relation-Preserving Scheme for Multiple-Scale Aeroacoustics Problems," *International Journal of Computational Fluid Dynamics*, Vol. 17, No. 2, 2003, pp. 119–132.

[27]Tam, C. K. W., "Computational Aeroacoustics: An Overview of Computational Challenges and Applications," *International Journal of Computational Fluid Dynamics*, Vol. 18, No. 6, 2004, pp. 547–567.

[28]Tam, C. K. W., Webb, J. C., and Dong, Z., "A Study of Short Wave Component in Computational Acoustics," *Journal of Computational Acoustics*, Vol. 1, No. 1, 1993, pp. 1–30.

[29]Tam, C. K. W., and Dong, Z., "Wall Boundary Conditions for High-Order Finite Difference Schemes in Computational Aeroacoustics," *Theoretical and Computational Fluid Dynamics*, Vol. 8, No. 5–6, 1994, pp. 303–322.

[30]Thomas, R. H., and Kinzie, K. W., "Jet-Pylon Interaction Effects for High Bypass Ratio Separate Flow and Chevron Nozzles," AIAA Paper 2004-2827, May 2004.

[31]Tam, C. K. W., and Auriault, L., "Mean Flow Refraction Effects on Sound Radiated from Localized Sources in a Jet," *Journal of Fluid Mechanics*, Vol. 370, 1998, pp. 149–174.

[32]Tam, C. K. W., Pastouchenko, N. N., and Schlinker, R. H., "On the Two Sources of Supersonic Jet Noise," AIAA Paper 2003-3163, Jan. 2003; also *Journal of Sound and Vibration* (to be published).

[33]Schlinker, R. H., "Supersonic Jet Noise Experiments," Ph.D. Dissertation, Dept. of Aerospace Engineering, Univ. of Southern California, Los Angeles, Aug. 1975.

[34]Laufer, J., Schlinker, R. H., and Kaplan, R. E., "Experiments on Supersonic Jet Noise," *AIAA Journal*, Vol. 14, No. 4, 1976, pp. 489–497.

C. Bailly
Associate Editor